

MULTILAYER GRAPHENE

I. SCALES OF THE HAMILTONIAN

We set $\hbar = 1$ throughout all the text. The UV cutoff \mathcal{K} of the system, fixed by the lattice parameter $2\pi/\mathcal{K}$, provides us a natural scale to measure the momenta, such that any momentum index \mathbf{k} is normalized by \mathcal{K} . In this way, we get the kinetic non-interacting Hamiltonian

$$H_{\text{kin}} = E_{\text{UV}} \sum_{\mathbf{k}\sigma\sigma'} \left(\frac{|\mathbf{k}|}{\mathcal{K}} \right)^m \psi_{\mathbf{k},\sigma}^\dagger \left(\hat{\mathbf{k}}_m \cdot \boldsymbol{\sigma}_{\sigma\sigma'} \right) \psi_{\mathbf{k},\sigma'}, \quad (1)$$

where $[\hat{\mathbf{k}}_m] = (\cos(m\phi_m) \sin(m\phi_m))$ and E_{UV} is the numerical value of the kinetic term evaluated at \mathcal{K} , and whose shape depends on m :

- $m = 1$: $E_{\text{UV}} = v\mathcal{K}$, where v is the Fermi velocity of the Dirac fermions.
- $m = 2$: $E_{\text{UV}} = \mathcal{K}^2/2m_e$, where m_e is the effective mass of the electron.

Therefore, the density of states per spin and per valley can be expressed as

$$N(E) = \frac{\mathcal{K}^2}{2\pi m} \sqrt{\frac{E^{2-m}}{E_{\text{UV}}^2}}, \quad (2)$$

which, as special cases:

- $m = 1$: $N(E) \propto (\mathcal{K}/E_{\text{UV}})^2 E = E/v^2$.
- $m = 2$: $N(E) \propto \mathcal{K}^2/E_{\text{UV}} = 2m_e$.

On the other hand, the interaction Hamiltonian can be expressed as

$$H_{\text{int}} = \frac{1}{2A} \sum_{\mathbf{k}\mathbf{k}'} \sum_{\sigma\sigma'} V_{\mathbf{q}} \psi_{\mathbf{k}'+\mathbf{q},\sigma'}^\dagger \psi_{\mathbf{k}-\mathbf{q},\sigma}^\dagger \psi_{\mathbf{k},\sigma} \psi_{\mathbf{k}',\sigma'}, \quad (3)$$

where A is the total area of the system.

II. RESTRICTED HILBERT SPACE FOR $\mathbf{Q} = 0$ EXCITONS AND PSEUDOSPIN BASIS

The optical relevant excitations of the system correspond to the $\mathbf{Q} = 0$ excitons, as shown in Fig. 1. These ones do not modify the momentum label of the electron when it jumps from the valence to the conduction band, and consequently, any interaction between a pair excitons at momenta \mathbf{k}_1 and \mathbf{k}_2 should only interchange their momentum labels. In other words, by having into account only $\mathbf{Q} = 0$ excitations, the Hilbert space of the system results restricted onto the singly-occupied sites in the momentum lattice. A good operator to describe the singly-occupied constrain is

$$s_{\mathbf{k}}^\mu = \sum_{\sigma\sigma'} \psi_{\mathbf{k},\sigma}^\dagger \sigma_{\sigma\sigma'}^\mu \psi_{\mathbf{k},\sigma'}. \quad (4)$$

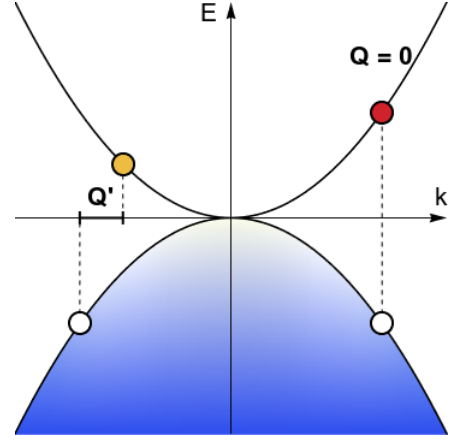


FIG. 1. $\mathbf{Q} = 0$ and $\mathbf{Q} \neq 0$ excitations on the parabolic bands.

where $\sigma_{\sigma,\sigma'}^\mu$ is the component $\sigma\sigma'$ of the matrix σ^μ , given by the generators of the $\text{SU}(2)$ Lie algebra, i.e., the Pauli matrices and the identity

$$\begin{aligned} \sigma^0 &= \begin{pmatrix} 1 & 0 \\ 0 & 1 \end{pmatrix}, & \sigma^1 &= \begin{pmatrix} 0 & 1 \\ 1 & 0 \end{pmatrix}, \\ \sigma^2 &= \begin{pmatrix} 0 & -i \\ i & 0 \end{pmatrix}, & \sigma^3 &= \begin{pmatrix} 1 & 0 \\ 0 & -1 \end{pmatrix}, \end{aligned} \quad (5)$$

The matrix σ^0 is useful to express the singly-occupied condition as the constrain

$$\begin{aligned} s_{\mathbf{k}}^0 &= \sum_{\sigma\sigma'} \psi_{\mathbf{k},\sigma}^\dagger \sigma_{\sigma\sigma'}^0 \psi_{\mathbf{k},\sigma'} = \sum_{\sigma\sigma'} \psi_{\mathbf{k},\sigma}^\dagger \delta_{\sigma\sigma'} \psi_{\mathbf{k},\sigma'} \\ &= \sum_{\sigma\sigma'} \psi_{\mathbf{k},\sigma}^\dagger \psi_{\mathbf{k},\sigma} = \sum_{\sigma} n_{\mathbf{k},\sigma} = 1. \end{aligned} \quad (6)$$

The following steps show how the four-fermion term in the interaction Hamiltonian can be expressed under the singly-occupied constrain. The completeness relation of the Pauli matrices

$$\sum_{\mu=0}^3 \sigma_{\sigma\sigma'}^\mu \sigma_{\tau\tau'}^\mu = 2\delta_{\sigma\tau} \delta_{\sigma'\tau'}, \quad (7)$$

and the trace of Pauli matrices bilinears

$$\text{tr} \left(\sigma^\mu \sigma^{\mu'} \right) = \sum_{\tau,\tau'} \sigma_{\tau\tau'}^\mu \sigma_{\tau'\tau}^{\mu'} = 2\delta^{\mu\mu'}, \quad (8)$$

are useful to find the inverse relation between fermion bilinears and Pauli matrices

$$\begin{aligned} \sum_{\mu=0}^3 \sigma_{\tau\tau'}^\mu s_{\mathbf{k}}^\mu &= \sum_{\mu=0}^3 \sum_{\sigma\sigma'} \psi_{\mathbf{k},\sigma}^\dagger \sigma_{\sigma\sigma'}^\mu \sigma_{\tau,\tau'}^\mu \psi_{\mathbf{k},\sigma'} \\ &= 2 \sum_{\sigma\sigma'} \psi_{\mathbf{k},\sigma}^\dagger \delta_{\sigma\tau} \delta_{\sigma'\tau} \psi_{\mathbf{k},\sigma'} \\ &= 2\psi_{\mathbf{k},\tau'}^\dagger \psi_{\mathbf{k},\tau}. \end{aligned} \quad (9)$$

In this way, the fermion bilinears can then be expanded in terms of the generators of the Lie algebra of the group $SU(2)$

$$\psi_{\mathbf{k},\tau'}^\dagger \psi_{\mathbf{k},\tau} = \frac{1}{2} \sum_{\mu=0}^3 s_{\mathbf{k}}^\mu \sigma_{\tau\tau'}^\mu, \quad (10)$$

The Eq. (10) is then useful to express the four-fermion term of the interaction Hamiltonian after some anticommutations to match fermion operators that share the same momentum label, such as follows

$$\begin{aligned} \sum_{\tau,\tau'} \left(\psi_{\mathbf{k},\tau}^\dagger \psi_{\mathbf{k},\tau'} \right) \left(\psi_{\mathbf{k}',\sigma}^\dagger \psi_{\mathbf{k}',\sigma'} \right) &= \\ &= \sum_{\tau,\tau'} \left(\frac{1}{2} \sum_{\mu=0}^3 \sigma_{\tau\tau'}^\mu s_{\mathbf{k}}^\mu \right) \left(\frac{1}{2} \sum_{\mu'=0}^3 \sigma_{\tau'\tau'}^{\mu'} s_{\mathbf{k}'}^{\mu'} \right) \\ &= \frac{1}{4} \sum_{\mu,\mu'} s_{\mathbf{k}}^\mu s_{\mathbf{k}'}^{\mu'} \sum_{\tau,\tau'} \sigma_{\tau\tau'}^\mu \sigma_{\tau'\tau'}^{\mu'} \\ &= \frac{1}{4} \sum_{\mu,\mu'} s_{\mathbf{k}}^\mu s_{\mathbf{k}'}^{\mu'} \text{tr} \left(\sigma^\mu \sigma^{\mu'} \right) \\ &= \frac{1}{2} \sum_{\mu,\mu'} s_{\mathbf{k}}^\mu s_{\mathbf{k}'}^{\mu'} \delta^{\mu\mu'} = \frac{1}{2} \sum_{\mu,\mu'} s_{\mathbf{k}}^\mu s_{\mathbf{k}'}^{\mu'} = \frac{1 + \mathbf{s}_{\mathbf{k}} \cdot \mathbf{s}_{\mathbf{k}'}}{2} \end{aligned} \quad (11)$$

Consequently, the original fermion Hamiltonian projected onto the singly-occupied is expressed as

$$\mathcal{P}H\mathcal{P} =$$

$$E_{UV} \sum_{\mathbf{k}} \left(\frac{|\mathbf{k}|}{\mathcal{K}} \right)^m \hat{\mathbf{k}}_m \cdot \mathbf{s}_{\mathbf{k}} - \sum_{\mathbf{k}_1 \neq \mathbf{k}_2} \frac{V_{\mathbf{k}_1 - \mathbf{k}_2}}{4A} \mathbf{s}_{\mathbf{k}_1} \cdot \mathbf{s}_{\mathbf{k}_2}, \quad (12)$$

where the first term represents a m -folded spin vortex (see Fig. 2) and the second term is an effective ferromagnetic exchange.

III. EXPANSION ABOUT THE NON-INTERACTING GROUND STATE

A. Band basis and interaction matrix

In this section, we provide details of the derivation of Eqs. (26) to (28) starting from Eq. (1). We begin describing the transformation from pseudo-spin basis onto band basis. In the band basis $s = \{+, -\}$ the kinetic term is:

$$\begin{aligned} \psi_{\mathbf{k}\sigma}^\dagger \left(\hat{\mathbf{k}}_m \cdot \boldsymbol{\sigma}_{\sigma\sigma'} \right) \psi_{\mathbf{k}\sigma'} &= \\ &= e^{-im\phi} \psi_{\mathbf{k}\uparrow}^\dagger \psi_{\mathbf{k}\downarrow} + e^{+im\phi} \psi_{\mathbf{k}\downarrow}^\dagger \psi_{\mathbf{k}\uparrow}. \end{aligned} \quad (13)$$

Band and pseudospin basis are related by:

$$\begin{aligned} \psi_{\mathbf{k}\sigma} &= \sum_s \langle \sigma | \mathbf{k}s \rangle \psi_{\mathbf{k}s}, \\ \begin{pmatrix} \psi_{\mathbf{k}\uparrow} \\ \psi_{\mathbf{k}\downarrow} \end{pmatrix} &= \frac{1}{\sqrt{2}} \begin{pmatrix} e^{-im\phi/2} & e^{-im\phi/2} \\ e^{+im\phi/2} & -e^{+im\phi/2} \end{pmatrix} \begin{pmatrix} \psi_{\mathbf{k}+} \\ \psi_{\mathbf{k}-} \end{pmatrix}. \end{aligned} \quad (14)$$

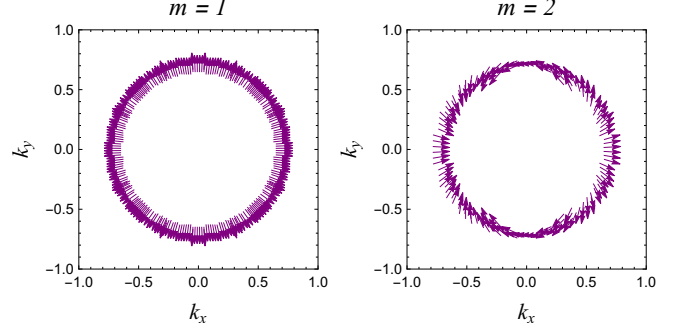


FIG. 2. Polar distribution of the vector $[\hat{\mathbf{k}}_m] = (\cos(m\phi_m), \sin(m\phi_m))$ used to describe the classical ground state of the system.

Fermion bilinears transform as

$$\sum_{\sigma} \psi_{\mathbf{k}_1\sigma}^\dagger \psi_{\mathbf{k}_2\sigma} = \psi_{\mathbf{k}_1 s_1}^\dagger \sum_{s_1 s_2} \langle \mathbf{k}_1 s_1 | \mathbf{k}_2 s_2 \rangle \psi_{\mathbf{k}_1 s_1}^\dagger \psi_{\mathbf{k}_2 s_2}, \quad (15)$$

where

$$\langle \mathbf{k}_1 s_1 | \mathbf{k}_2 s_2 \rangle = \begin{pmatrix} \cos m\phi_{12}/2 & i \sin m\phi_{12}/2 \\ i \sin m\phi_{12}/2 & \cos m\phi_{12}/2 \end{pmatrix}, \quad (16)$$

where ϕ_i is the polar angle of \mathbf{k}_i , and $\phi_{12} = \phi_1 - \phi_2$. Therefore, the Hamiltonian in Eq. (1) of the Main text in the band basis is expressed as follows:

$$\begin{aligned} \mathcal{P}H\mathcal{P} &= \sum_{\mathbf{k}} E_{\mathbf{k}}^m \left(\psi_{\mathbf{k}+}^\dagger \psi_{\mathbf{k}+} - \psi_{\mathbf{k}-}^\dagger \psi_{\mathbf{k}-} \right) \\ &- \sum_{\mathbf{k}_1 \neq \mathbf{k}_2} \sum_{s_1 s_2} (T_{\mathbf{k}_1 \mathbf{k}_2}^m)^{s_1 s_2} \psi_{\mathbf{k}_1 s_1}^\dagger \psi_{\mathbf{k}_1 \bar{s}_1} \psi_{\mathbf{k}_2 \bar{s}_2}^\dagger \psi_{\mathbf{k}_2 s_2}, \end{aligned} \quad (17)$$

where $E_{\mathbf{k}}^m = E_{UV}(|\mathbf{k}|/\mathcal{K})^m + \Sigma_{\mathbf{k}}^m$ is the effective dispersion relation of the electrons, in which $\Sigma_{\mathbf{k}}^m$ is the self-energy

$$\Sigma_{\mathbf{k}}^m = \frac{1}{2A} \sum_{\mathbf{p}} V_{\mathbf{k}-\mathbf{p}} \cos(m\phi_{\mathbf{k}\mathbf{p}}). \quad (18)$$

and $(T_{\mathbf{k}_1 \mathbf{k}_2}^m)^{s_1 s_2}$ is the interaction matrix in the band basis, given by:

$$T_{\mathbf{k}_1 \mathbf{k}_2}^m = \frac{V_{\mathbf{k}_1 - \mathbf{k}_2}}{4A} \begin{pmatrix} 1 + \cos(m\phi_{12}) & 1 - \cos(m\phi_{12}) \\ 1 - \cos(m\phi_{12}) & 1 + \cos(m\phi_{12}) \end{pmatrix}. \quad (19)$$

B. Holstein-Primakoff expansion

We select the following spin basis

$$\mathbf{s}_{\mathbf{k}} = -s_{\mathbf{k}}^z \hat{\mathbf{k}}_m + s_{\mathbf{k}}^x \hat{\mathbf{z}} + s_{\mathbf{k}}^y \hat{\phi}_m, \quad (20)$$

which diagonalizes the kinetic term, and where $\hat{\mathbf{z}}$ is the normal axis to the layer and $\hat{\phi}_m = \hat{\mathbf{z}} \times \hat{\mathbf{k}}_m =$

$(-\sin(m\phi_m)\cos(m\phi_m))$, and the exchange term is expanded as

$$\begin{aligned} \hat{\mathbf{s}}_{\mathbf{k}} \cdot \hat{\mathbf{s}}_{\mathbf{k}'} &= \left(-\hat{s}_{\mathbf{k}_1}^z \hat{\mathbf{k}} + \hat{s}_{\mathbf{k}}^x \hat{\mathbf{z}} + \hat{s}_{\mathbf{k}}^y \hat{\boldsymbol{\varphi}} \right) \cdot \left(-\hat{s}_{\mathbf{k}'}^z \hat{\mathbf{k}}' + \hat{s}_{\mathbf{k}'}^x \hat{\mathbf{z}} + \hat{s}_{\mathbf{k}'}^y \hat{\boldsymbol{\varphi}}' \right) \\ &= (\hat{s}_{\mathbf{k}}^z \hat{s}_{\mathbf{k}'}^z + \hat{s}_{\mathbf{k}}^x \hat{s}_{\mathbf{k}'}^x) \cos \phi_{\mathbf{k}\mathbf{k}'} + \hat{s}_{\mathbf{k}}^y \hat{s}_{\mathbf{k}'}^y \\ &\quad + (\hat{s}_{\mathbf{k}}^y \hat{s}_{\mathbf{k}'}^z - \hat{s}_{\mathbf{k}}^z \hat{s}_{\mathbf{k}'}^y) \sin \phi_{\mathbf{k}\mathbf{k}'} \end{aligned} \quad (21)$$

with $\cos \phi_{\mathbf{k}\mathbf{k}'} = \hat{\mathbf{k}} \cdot \hat{\mathbf{k}}' = \hat{\boldsymbol{\varphi}} \cdot \hat{\boldsymbol{\varphi}}'$. On this basis, the Hamiltonian can be expanded in a bosonic representation by means of the Holstein-Primakoff (HP) transformations ($S = 1/2$):

$$\begin{aligned} s_{\mathbf{k}}^z &= 2 \left(S - b_{\mathbf{k}}^\dagger b_{\mathbf{k}} \right) = 1 - 2b_{\mathbf{k}}^\dagger b_{\mathbf{k}}, \\ s_{\mathbf{k}}^x &\approx \sqrt{2S} \left(b_{\mathbf{k}} + b_{\mathbf{k}}^\dagger \right) = b_{\mathbf{k}} + b_{\mathbf{k}}^\dagger, \\ i s_{\mathbf{k}}^y &\approx \sqrt{2S} \left(b_{\mathbf{k}} - b_{\mathbf{k}}^\dagger \right) = b_{\mathbf{k}} - b_{\mathbf{k}}^\dagger. \end{aligned} \quad (22)$$

The term corresponding to the exchange coupling in Eq. (12) can be transformed into pairing and hopping terms of bosons up to bilinears:

$$\begin{aligned} \mathbf{s}_{\mathbf{k}} \cdot \mathbf{s}_{\mathbf{k}'} &\approx \left(1 + b_{\mathbf{k}}^\dagger b_{\mathbf{k}} + b_{\mathbf{k}'}^\dagger b_{\mathbf{k}'} \right) \cos \phi_{\mathbf{k}\mathbf{k}'} \\ &\quad + \left(b_{\mathbf{k}}^\dagger b_{\mathbf{k}'} + b_{\mathbf{k}} b_{\mathbf{k}'}^\dagger \right) (1 + \cos \phi_{\mathbf{k}\mathbf{k}'}) \\ &\quad + \left(b_{\mathbf{k}}^\dagger b_{\mathbf{k}'}^\dagger + b_{\mathbf{k}} b_{\mathbf{k}'} \right) (1 - \cos \phi_{\mathbf{k}\mathbf{k}'}) \\ &\quad + i \left(b_{\mathbf{k}}^\dagger - b_{\mathbf{k}'}^\dagger - b_{\mathbf{k}} + b_{\mathbf{k}'} \right) \sin \phi_{\mathbf{k}\mathbf{k}'} . \end{aligned} \quad (23)$$

The resulting bosonic Hamiltonian after applying the HP transformations is:

$$\begin{aligned} H_{HP} &= \sum_{\mathbf{k}} 2E_{UV} \left(\frac{|\mathbf{k}|}{\mathcal{K}} \right)^m b_{\mathbf{k}}^\dagger b_{\mathbf{k}} + \sum_{\mathbf{k} \neq \mathbf{p}} \frac{V_{\mathbf{k}-\mathbf{p}}}{A} b_{\mathbf{k}}^\dagger b_{\mathbf{k}} \cos(m\phi_{\mathbf{k}\mathbf{p}}) \\ &\quad + \sum_{\mathbf{k} \neq \mathbf{k}'} \frac{V_{\mathbf{k}-\mathbf{k}'}}{4A} (1 + \cos(m\phi_{\mathbf{k}_1\mathbf{k}_2})) \left(b_{\mathbf{k}_1}^\dagger b_{\mathbf{k}_2} + b_{\mathbf{k}_1} b_{\mathbf{k}_2}^\dagger \right) + \\ &\quad + \sum_{\mathbf{k} \neq \mathbf{k}'} \frac{V_{\mathbf{k}-\mathbf{k}'}}{4A} (1 - \cos(m\phi_{\mathbf{k}_1\mathbf{k}_2})) \left(b_{\mathbf{k}_1}^\dagger b_{\mathbf{k}_2}^\dagger + b_{\mathbf{k}_1} b_{\mathbf{k}_2} \right). \end{aligned} \quad (24)$$

The first line contains the kinetic and self-energy terms. The second line can be viewed as boson hopping terms in the momentum lattice. The third line can be viewed as pairing terms which change the number of bosons. Lastly, by using the Bogoliubov basis given by

$$B_{\mathbf{k}}^\dagger = \left(b_{\mathbf{k}}^\dagger \quad b_{\mathbf{k}} \right), \quad (25)$$

the Hamiltonian can be expressed as

$$H_{HP} = \sum_{\mathbf{k}_1, \mathbf{k}_2} B_{\mathbf{k}_1}^\dagger H_{\mathbf{k}_1\mathbf{k}_2} B_{\mathbf{k}_2}, \quad (26)$$

with $B_{\mathbf{k}}^\dagger = \left(b_{\mathbf{k}}^\dagger \quad b_{\mathbf{k}} \right)$, and

$$H_{\mathbf{k}_1\mathbf{k}_2} = \delta_{\mathbf{k}_1\mathbf{k}_2} \begin{pmatrix} 2E_{\mathbf{k}_1}^m & 0 \\ 0 & -2E_{\mathbf{k}_1}^m \end{pmatrix} - T_{\mathbf{k}_1\mathbf{k}_2}^m, \quad (27)$$

with $E_{\mathbf{k}} = v|\mathbf{k}| + \Sigma_{\mathbf{k}}$, $\Sigma_{\mathbf{k}} = \sum_{\mathbf{k}'} V_{\mathbf{k}-\mathbf{k}'} \cos(m\phi_{\mathbf{k}\mathbf{k}'})/2A$ is the Hartree-Fock self-energy, $T_{\mathbf{k}\mathbf{k}'}$ is

$$T_{\mathbf{k}\mathbf{k}'} = \frac{V_{\mathbf{k}-\mathbf{k}'}}{4A} \begin{pmatrix} 1 + \cos(m\phi_{\mathbf{k}\mathbf{k}'}) & 1 - \cos(m\phi_{\mathbf{k}\mathbf{k}'}) \\ 1 - \cos(m\phi_{\mathbf{k}\mathbf{k}'}) & 1 + \cos(m\phi_{\mathbf{k}\mathbf{k}'}) \end{pmatrix}. \quad (28)$$

IV. ELECTRON-ELECTRON POTENTIALS

The system is explored using two different kinds of potentials: a Gaussian-shaped potential and a Coulombic potential. The next two sections explore their Fourier transforms and define their parameters essential for the numerical exploration of the Hamiltonian.

A. Gaussian potential

The potential is given by

$$V_{\mathbf{r}} = V_0 e^{-r^2/2a^2} \quad (29)$$

with V_0 the intensity of the Gaussian potential and a the spreading in the real space. Its 2D Fourier transform is

$$\begin{aligned} V_{\mathbf{k}} &= a^2 V_0 e^{-\frac{a^2 k^2}{2}} = \frac{E_{UV}}{\mathcal{K}^2} \left[\frac{(a\mathcal{K})^2 V_0}{E_{UV}} e^{-\frac{(a\mathcal{K})^2}{2} \left(\frac{k}{\mathcal{K}} \right)^2} \right], \\ V_{\mathbf{k}} &= \frac{E_{UV}}{\mathcal{K}^2} \left(g_{\mathcal{K}} e^{-\frac{a_{\mathcal{K}}^2}{2} \left(\frac{k}{\mathcal{K}} \right)^2} \right), \end{aligned} \quad (30)$$

where $k = |\mathbf{k}|$. Notice the expression of the density of states for bilayer graphene as a normalization constant. It is assumed that $a > 2\pi/\mathcal{K}$, i.e., the spreading of the Gaussian should be larger than the lattice parameter $2\pi/\mathcal{K}$. The additional two nondimensional parameters are:

- Reciprocal spreading $a_{\mathcal{K}} = a\mathcal{K}$: Determines how concentrated is the potential in the reciprocal space. $a_{\mathcal{K}}$ is constrained to be larger than one.
- Coupling constant $g_{\mathcal{K}} = a_{\mathcal{K}}^2 V_0/E_{UV}$: Relates the intensity of the Gaussian potential in the reciprocal space to E_{UV} , the kinetic energy at the UV cutoff.

Then, the interaction Hamiltonian turns out to be

$$\begin{aligned} H_{\text{int}} &= \frac{1}{2A} \sum_{\mathbf{k}\mathbf{k}'} \sum_{\sigma\sigma'} V_{\mathbf{q}} \psi_{\mathbf{k}'+\mathbf{q},\sigma'}^\dagger \psi_{\mathbf{k}-\mathbf{q},\sigma}^\dagger \psi_{\mathbf{k},\sigma} \psi_{\mathbf{k}',\sigma'} \\ &= \frac{E_{UV}}{2A\mathcal{K}^2} \sum_{\mathbf{k}\mathbf{k}'} \sum_{\sigma\sigma'} g_{\mathcal{K}} e^{-\frac{a_{\mathcal{K}}^2}{2} \left(\frac{k}{\mathcal{K}} \right)^2} \psi_{\mathbf{k}'+\mathbf{q},\sigma'}^\dagger \psi_{\mathbf{k}-\mathbf{q},\sigma}^\dagger \psi_{\mathbf{k},\sigma} \psi_{\mathbf{k}',\sigma'}. \end{aligned} \quad (31)$$

where A is the total area of the system.

B. Coulombic potential

The potential is given by

$$V_{\mathbf{r}} = \frac{2\pi e^2}{\kappa} \left(\frac{1}{\sqrt{r^2 + \mathcal{K}^{-2}}} - \frac{1}{\sqrt{r^2 + a^2}} \right) \quad (32)$$

with e the elementary electric charge, κ is the substrate dielectric constant and a is a short distance limit that plays the role of an IR cutoff. Its 2D Fourier transform is

$$\begin{aligned} V_{\mathbf{k}} &= \frac{2\pi e^2}{\kappa} \frac{e^{-\left(\frac{k}{\mathcal{K}}\right)} - e^{-ak}}{k} = \frac{2\pi e^2}{\kappa \mathcal{K}} \frac{e^{-\left(\frac{k}{\mathcal{K}}\right)} - e^{-a\mathcal{K}\left(\frac{k}{\mathcal{K}}\right)}}{k/\mathcal{K}} \\ &= \frac{E_{UV}}{\mathcal{K}^2} \left[\frac{2\pi e^2 \mathcal{K}}{\kappa E_{UV}} \frac{e^{-\left(\frac{k}{\mathcal{K}}\right)} - e^{-a\mathcal{K}\left(\frac{k}{\mathcal{K}}\right)}}{k/\mathcal{K}} \right] \\ V_{\mathbf{k}} &= \frac{E_{UV}}{\mathcal{K}^2} \left(g_{\mathcal{K}} \frac{e^{-\left(\frac{k}{\mathcal{K}}\right)} - e^{-a\mathcal{K}\left(\frac{k}{\mathcal{K}}\right)}}{k/\mathcal{K}} \right), \end{aligned} \quad (33)$$

where $k = |\mathbf{k}|$. Note once again the expression of the density of states for bilayer graphene as a normalization constant. It is assumed that $a > 2\pi/\mathcal{K}$, i.e., the IR cutoff of the mirror Coulomb potential should be larger than the UV cutoff \mathcal{K} . The additional two nondimensional parameters are:

- Reciprocal spreading $a_{\mathcal{K}} = a\mathcal{K}$: Determines the IR cutoff in terms of the UV cutoff \mathcal{K} . As well as in the Gaussian case, $a_{\mathcal{K}}$ is constrained to be larger than one.
- Coupling constant $g_{\mathcal{K}} = 2\pi e^2 \mathcal{K} / \kappa E_{UV}$: Relates the intensity of the Coulomb potential, $2\pi e^2 / \kappa$ with units of velocity, to E_{UV} / \mathcal{K} , half the velocity at the UV cutoff.

Then, the interaction Hamiltonian turns out to be

$$\begin{aligned} H_{\text{int}} &= \frac{1}{2A} \sum_{\mathbf{k}\mathbf{k}'} \sum_{\sigma\sigma'} V_{\mathbf{q}} \psi_{\mathbf{k}'+\mathbf{q},\sigma'}^\dagger \psi_{\mathbf{k}-\mathbf{q},\sigma}^\dagger \psi_{\mathbf{k},\sigma} \psi_{\mathbf{k}',\sigma'} \\ &= \frac{E_{UV}}{2A\mathcal{K}^2} \sum_{\mathbf{k}\mathbf{k}'} \sum_{\sigma\sigma'} g_{\mathcal{K}} \left(\frac{e^{-\left(\frac{k}{\mathcal{K}}\right)} - e^{-a\mathcal{K}\left(\frac{k}{\mathcal{K}}\right)}}{k/\mathcal{K}} \right) \times \\ &\quad \times \psi_{\mathbf{k}'+\mathbf{q},\sigma'}^\dagger \psi_{\mathbf{k}-\mathbf{q},\sigma}^\dagger \psi_{\mathbf{k},\sigma} \psi_{\mathbf{k}',\sigma'}. \end{aligned} \quad (34)$$

where A is the total area of the system.

V. HARTREE-FOCK SELF-ENERGY IN MULTILAYER GRAPHENE

The Hartree-Fock self-energy of the electrons and holes is given by

$$\Sigma^m(\mathbf{k}) = \int \frac{d^2\mathbf{p}}{(2\pi)^2} V(\mathbf{k} - \mathbf{p}) \cos(m\phi_{\mathbf{k}\mathbf{p}}), \quad (35)$$

where $V(\mathbf{k} - \mathbf{p})$ is replaced by the expressions of the Fourier transforms for the Gaussian and the Coulomb potentials.

A. Gaussian Potential

The Fourier potential in (30) is then replaced in (35)

$$\Sigma^m(\mathbf{k}) = \frac{E_{UV}}{\mathcal{K}^2} \int \frac{d^2\mathbf{p}}{(2\pi)^2} g_{\mathcal{K}} e^{-\frac{a_{\mathcal{K}}^2}{2} \left(\frac{\mathbf{k}-\mathbf{p}}{\mathcal{K}} \right)^2} \cos(m\phi_{\mathbf{k}\mathbf{p}}), \quad (36)$$

In order to get an analytic expression for $\Sigma^m(\mathbf{k})$, it is defined the following integral as

$$I(k) = \int \frac{pd\phi}{(2\pi)^2} e^{-\left(\frac{k^2+p^2-2kp\cos\phi}{2}\right)} \cos(m\phi), \quad (37)$$

and, after substituting $x = a_{\mathcal{K}}p/\mathcal{K}$ and $y = a_{\mathcal{K}}k/\mathcal{K}$,

$$\begin{aligned} I(k) &= \frac{\mathcal{K}^2}{a_{\mathcal{K}}^2} \int \frac{xdx d\phi}{(2\pi)^2} e^{-\left(\frac{x^2+y^2-2xy\cos\phi}{2}\right)} \cos(m\phi) \\ &= \frac{\mathcal{K}^2}{a_{\mathcal{K}}^2} \int \frac{xdx}{2\pi} e^{-\frac{x^2+y^2}{2}} \int \frac{d\phi}{2\pi} e^{xy\cos\phi} \cos(m\phi), \end{aligned} \quad (38)$$

The polar integral is done using the Jacobi-Anger identity

$$e^{i\zeta \cos\phi} = \sum_{n=-\infty}^{+\infty} i^n J_n(\zeta) e^{in\phi} = J_0(\zeta) + 2 \sum_{n=1}^{\infty} i^n J_n(\zeta) \cos(n\phi),$$

with imaginary argument $i\zeta = z$

$$e^{z \cos\phi} = \sum_{n=-\infty}^{+\infty} I_n(z) e^{in\phi} = J_0(z) + 2 \sum_{n=1}^{\infty} I_n(z) \cos(n\phi), \quad (39)$$

so that

$$\begin{aligned} &\int \frac{d\phi}{2\pi} e^{xy\cos\phi} \cos(m\phi) \\ &= \int \frac{d\phi}{2\pi} \left(I_0(xy) + 2 \sum_{n=1}^{\infty} I_n(xy) \cos(n\phi) \right) \cos(m\phi) \\ &= 2 \sum_{n=1}^{\infty} I_n(xy) \left(\int \frac{d\phi}{2\pi} \cos(n\phi) \cos(m\phi) \right) \\ &= \sum_{n=1}^{\infty} I_n(xy) \delta_{nm} = I_m(xy), \end{aligned} \quad (40)$$

Substituting $I_m(xy)$ in the self-energy integral in Eq. (38) yields

$$\begin{aligned} I(k) &= \frac{\mathcal{K}^2}{a_{\mathcal{K}}^2} \int \frac{xdx}{2\pi} e^{-\frac{x^2+y^2}{2}} \int \frac{d\phi}{2\pi} e^{xy\cos\phi} \cos(m\phi) \\ &= \frac{\mathcal{K}^2}{a_{\mathcal{K}}^2} \int \frac{xdx}{2\pi} e^{-\frac{x^2+y^2}{2}} I_m(xy) \\ &= \frac{\mathcal{K}^2}{a_{\mathcal{K}}^2} \frac{ye^{-\frac{y^2}{2}}}{4\sqrt{2\pi}} \left[I_{\frac{m-1}{2}} \left(\frac{y^2}{4} \right) + I_{\frac{m+1}{2}} \left(\frac{y^2}{4} \right) \right], \end{aligned} \quad (41)$$

Finally, the self-energy of the m -layer graphene is then expressed as

$$\Sigma^m(\mathbf{k}) = \frac{g_K E_{UV}}{8a_K} \frac{ke^{-\frac{a_K^2 k^2}{4K^2}}}{\mathcal{K}\sqrt{2\pi}} \times \left[I_{\frac{m-1}{2}} \left(\frac{a_K^2 k^2}{4K^2} \right) + I_{\frac{m+1}{2}} \left(\frac{a_K^2 k^2}{4K^2} \right) \right], \quad (42)$$

The two limit cases for large and small momenta are given by the following expressions:

$$\begin{aligned} \lim_{k \rightarrow \infty} \Sigma^m(\mathbf{k}) &= \frac{E_{UV}}{4\pi a_K^2} \\ \lim_{k \rightarrow 0} \Sigma^m(\mathbf{k}) &= \frac{2^{-\frac{3m+4}{2}} E_{UV} \left(\frac{a_K k}{K} \right)^m}{\sqrt{\pi} a_K^2 \Gamma \left(\frac{m+1}{2} \right)} \end{aligned} \quad (43)$$

As special cases, the self-energy corresponding to any odd number of layers and bilayer graphene are

$$\Sigma^n(\mathbf{k}) = \frac{g_K E_{UV}}{8a_K} \frac{ke^{-\frac{a_K^2 k^2}{4K^2}}}{\mathcal{K}\sqrt{2\pi}} \left[I_n \left(\frac{a_K^2 k^2}{4K^2} \right) + I_{n+1} \left(\frac{a_K^2 k^2}{4K^2} \right) \right], \quad (44)$$

$$\begin{aligned} \Sigma^2(\mathbf{k}) &= \frac{g_K E_{UV}}{8a_K} \frac{ke^{-\frac{a_K^2 k^2}{4K^2}}}{\mathcal{K}\sqrt{2\pi}} \left[I_{\frac{1}{2}} \left(\frac{a_K^2 k^2}{4K^2} \right) + I_{\frac{3}{2}} \left(\frac{a_K^2 k^2}{4K^2} \right) \right] \\ &= \frac{g_K E_{UV}}{4\pi a_K^2} \left[1 - \frac{2K^2}{a_K^2 k^2} \left(1 - e^{-\frac{a_K^2 k^2}{4K^2}} \right) \right], \end{aligned} \quad (45)$$

where n is an odd integer (see the Fig. 3 for the cases of monolayer, bilayer and trilayer graphene). Their corresponding small-momentum regimes are described by

$$\begin{aligned} \Sigma^1(\mathbf{k}) &\approx \frac{g_K E_{UV}}{8\sqrt{2\pi} a_K} \left(\frac{k}{K} \right) + O(k^2), \\ \Sigma^2(\mathbf{k}) &\approx \frac{g_K E_{UV}}{16\pi} \left(\frac{k}{K} \right)^2 + O(k^3), \\ \Sigma^3(\mathbf{k}) &\approx \frac{a_K E_{UV}}{64\sqrt{2}\sqrt{\pi}} \left(\frac{k}{K} \right)^3 + O(k^4), \end{aligned} \quad (46)$$

Notice that the dependence on a_K of the lowest-expansion-term coefficient for $\Sigma^1(\mathbf{k})$ is inverse to the dependence of $\Sigma^3(\mathbf{k})$. Even more, the lowest-expansion-term coefficient for $\Sigma^2(\mathbf{k})$ is independent of a_K , as it is shown in Fig. 4.

B. Coulombic Potential

The Fourier potential in (33) is then replaced in (35)

$$\begin{aligned} \Sigma^m(\mathbf{k}) &= \frac{E_{UV}}{K^2} \int \frac{d^2 \mathbf{p}}{(2\pi)^2} \times \\ &\times g_K \left(\frac{e^{-\left(\frac{|\mathbf{k}-\mathbf{p}|}{K} \right)} - e^{-a_K \left(\frac{|\mathbf{k}-\mathbf{p}|}{K} \right)}}{|\mathbf{k}-\mathbf{p}|/K} \right) \cos(m\phi_{\mathbf{k}\mathbf{p}}), \end{aligned} \quad (47)$$

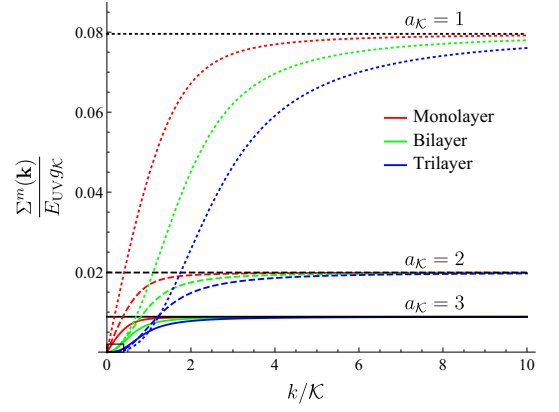


FIG. 3. Hartree-Fock self-energy $\Sigma^m(\mathbf{k})$ for monolayer ($m = 1$, red), bilayer ($m = 2$, green) and trilayer ($m = 3$, blue) graphene. The dasheding of the plots represent the value of the spreading parameter: $a_K = 1$ (dotted), a_K (dashed), and $a_K = 3$ (solid), while the horizontal black lines represent the asymptotic limit $\Sigma^m(\infty)$ the three values of a_K . The little rectangle at the origin is zoomed in Fig. 4.

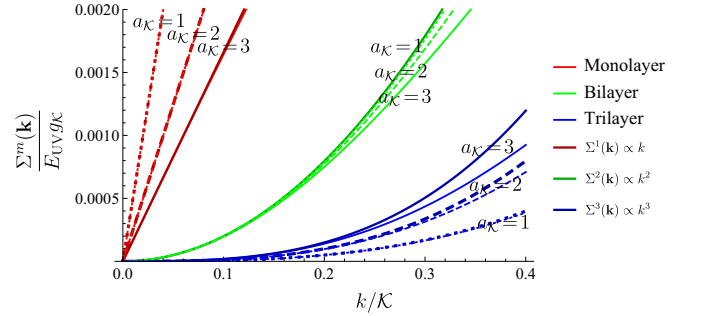


FIG. 4. Low-momentum limit for $\Sigma^m(\mathbf{k})$ in monolayer, bilayer and trilayer graphene. The legends are the same shown in Fig. 3 with the additional bolded curves representing the lowest-order expansion terms and labels of a_K to help with the interpretation of the plot. Notice that the low-momentum limit of $\Sigma^2(\mathbf{k})$ is independent of a_K .

The self-energy of the m -layer graphene is then expressed as

$$\begin{aligned} \Sigma^m(\mathbf{k}) &= \frac{g_K E_{UV} k}{4K} \times \\ &\times \left[I_{\frac{m-1}{2}} \left(\frac{k}{2K} \right) K_{\frac{m-1}{2}} \left(\frac{k}{2K} \right) + I_{\frac{m+1}{2}} \left(\frac{k}{2K} \right) K_{\frac{m+1}{2}} \left(\frac{k}{2K} \right) \right], \end{aligned} \quad (48)$$

The two limit cases for large and small momenta are given by the following expressions:

$$\begin{aligned} \lim_{k \rightarrow \infty} \Sigma^m(\mathbf{k}) &= \frac{g_K E_{UV}}{2} \\ \lim_{k \rightarrow 0} \Sigma^m(\mathbf{k}) &= \frac{m g_K E_{UV}}{2(m^2 - 1)} \left(\frac{k}{K} \right), \quad m > 1, \end{aligned} \quad (49)$$

It is found a similar behavior for large momenta like the Gaussian potential, but for small momenta, excepting

$m = 1$, the leading order is always linear in k/K , regardless the number of layers m , highly in contrast to the Gaussian case where the leading order is proportional to $(k/K)^m$.

ARREGLAR EXPRESIONES Y EXPLICAR EL CASO $m = 1$

As special cases, the self-energy corresponding to any odd-layer and bilayer graphene are

$$\Sigma^n(\mathbf{k}) = \frac{g_K E_{UV}}{8a_K} \frac{ke^{-\frac{a_K^2 k^2}{4K^2}}}{K\sqrt{2\pi}} \left[I_n \left(\frac{a_K^2 k^2}{4K^2} \right) + I_{n+1} \left(\frac{a_K^2 k^2}{4K^2} \right) \right], \quad (50)$$

$$\begin{aligned} \Sigma^2(\mathbf{k}) &= \frac{g_K E_{UV}}{8a_K} \frac{ke^{-\frac{a_K^2 k^2}{4K^2}}}{K\sqrt{2\pi}} \left[I_{\frac{1}{2}} \left(\frac{a_K^2 k^2}{4K^2} \right) + I_{\frac{3}{2}} \left(\frac{a_K^2 k^2}{4K^2} \right) \right] \\ &= \frac{g_K E_{UV}}{4\pi a_K^2} \left[1 - \frac{2K^2}{a_K^2 k^2} \left(1 - e^{-\frac{a_K^2 k^2}{4K^2}} \right) \right], \end{aligned} \quad (51)$$

where n is an odd integer (see the Fig. 3 for the cases of monolayer, bilayer and trilayer graphene). Their corresponding small-momentum regimes are described by

$$\begin{aligned} \Sigma^1(\mathbf{k}) &\approx \frac{g_K E_{UV}}{8\sqrt{2\pi} a_K} \left(\frac{k}{K} \right) + O(k^2), \\ \Sigma^2(\mathbf{k}) &\approx \frac{g_K E_{UV}}{16\pi} \left(\frac{k}{K} \right)^2 + O(k^3), \\ \Sigma^3(\mathbf{k}) &\approx \frac{a_K E_{UV}}{64\sqrt{2}\sqrt{\pi}} \left(\frac{k}{K} \right)^3 + O(k^4), \end{aligned} \quad (52)$$

Notice that the dependence on a_K of the lowest-expansion-term coefficient for $\Sigma^1(\mathbf{k})$ is inverse to the dependence of $\Sigma^3(\mathbf{k})$. Even more, the lowest-expansion-term coefficient for $\Sigma^2(\mathbf{k})$ is independent of a_K , as it is shown in Fig. 4.

VI. ANGULAR MOMENTUM CHANNELS AND PARAMETRIZATION OF THE RADIAL COORDINATE

A. General coordinate transformations on the continuum limit

We begin by taking the continuum limit of the Hamiltonian in the Bogoliubov basis (26), for this purpose it is convenient to define a rescaled Hamiltonian and boson creation operator as follows:

$$\begin{aligned} B(\mathbf{k}) &\equiv \lim_{\Delta k \rightarrow 0} \frac{B_{\mathbf{k}}}{\sqrt{\Delta k_x \Delta k_y}}, \\ H(\mathbf{k}, \mathbf{k}') &\equiv \lim_{\Delta k \rightarrow 0} \frac{H_{\mathbf{k}\mathbf{k}'}}{\Delta k_x \Delta k_y}, \end{aligned} \quad (53)$$

where $\Delta k_{x,y} = 2\pi/\sqrt{A}$, A is the system area that we take to be a square. The above re-definitions allow to obtain

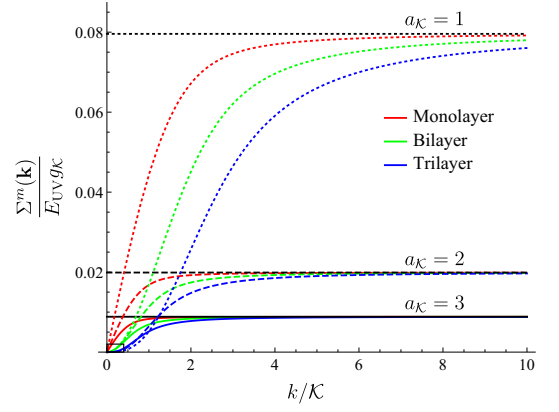


FIG. 5. Hartree-Fock self-energy $\Sigma^m(\mathbf{k})$ for monolayer ($m = 1$, red), bilayer ($m = 2$, green) and trilayer ($m = 3$, blue) graphene. The dasheding of the plots represent the value of the spreading parameter: $a_K = 1$ (dotted), a_K (dashed), and $a_K = 3$ (solid), while the horizontal black lines represent the asymptotic limit $\Sigma^m(\infty)$ the three values of a_K . The little rectangle at the origin is zoomed in Fig. 4.

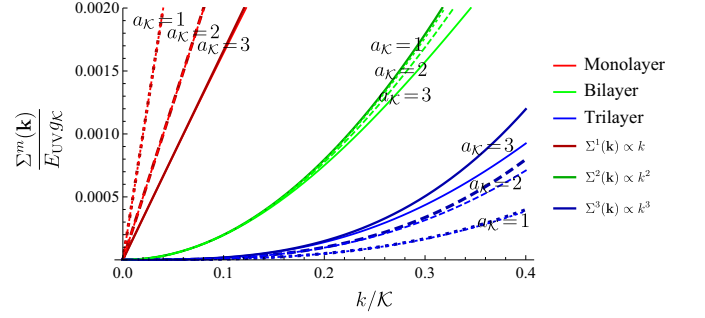


FIG. 6. Low-momentum limit for $\Sigma^m(\mathbf{k})$ in monolayer, bilayer and trilayer graphene. The legends are the same shown in Fig. 3 with the additional bolded curves representing the lowest-order expansion terms and labels of a_K to help with the interpretation of the plot. Notice that the low-momentum limit of $\Sigma^2(\mathbf{k})$ is independent of a_K .

the following continuum commutation relations for the boson operators:

$$[B(\mathbf{k}), B^\dagger(\mathbf{k}')] = \lim_{\Delta k \rightarrow 0} \mathbb{I} \frac{\delta_{\mathbf{k}\mathbf{k}'}}{(\Delta k)^2} = \mathbb{I} \delta^2(\mathbf{k} - \mathbf{k}'),$$

where

$$\mathbb{I} = \begin{pmatrix} 1 & 0 \\ 0 & -1 \end{pmatrix}. \quad (54)$$

With these rescalings we can convert the sums over momenta into continuum integrals, obtaining the continuum

version of the boson Hamiltonian H_{HP} from Eq. (26):

$$\begin{aligned}\mathcal{H}_{HP} &= \lim_{\Delta k \rightarrow 0} \int \frac{d^2 k}{(\Delta k)^2} \frac{d^2 k'}{(\Delta k)^2} B_{\mathbf{k}}^\dagger H_{\mathbf{k}\mathbf{k}'} B_{\mathbf{k}'} \\ &= \lim_{\Delta k \rightarrow 0} (\Delta k)^4 \int \frac{d^2 k}{(\Delta k)^2} \frac{d^2 k'}{(\Delta k)^2} B_\sigma^\dagger(\mathbf{k}) H(\mathbf{k}, \mathbf{k}') B_\sigma(\mathbf{k}') \\ &= \int d^2 k d^2 k' \hat{B}_\sigma^\dagger(\mathbf{k}) H(\mathbf{k}, \mathbf{k}') \hat{B}_\sigma(\mathbf{k}').\end{aligned}$$

From this continuum Hamiltonian we can perform a change of coordinates $\mathbf{z}(\mathbf{k})$ with Jacobian $D(\mathbf{z}) = |\frac{\partial \mathbf{k}}{\partial \mathbf{z}}|$ with the following redefinitions:

$$\begin{aligned}B(\mathbf{z}) &= \sqrt{D(\mathbf{z})} B(\mathbf{k}(\mathbf{z})), \\ H(\mathbf{z}, \mathbf{z}') &= \sqrt{D(\mathbf{z}) D(\mathbf{z}')} H(\mathbf{k}(\mathbf{z}), \mathbf{k}(\mathbf{z}')), \end{aligned} \quad (55)$$

whose purpose is to maintain the same form of the commutation relations and the Hamiltonian as follows:

$$\begin{aligned}[B(\mathbf{z}), B^\dagger(\mathbf{z}')] &= \mathbb{I} \delta^2(\mathbf{z} - \mathbf{z}'), \\ \mathcal{H}_{HP} &= \int d^2 z d^2 z' \hat{B}_\sigma^\dagger(\mathbf{z}) H(\mathbf{z}, \mathbf{z}') \hat{B}_\sigma(\mathbf{z}').\end{aligned}$$

Lastly, on the new coordinate system, we proceed to re-discretize the expressions, as follows:

$$\begin{aligned}B_{\mathbf{z}} &\leftarrow \sqrt{\Delta z_1 \Delta z_2} B(\mathbf{z}), \\ H_{\mathbf{z}, \mathbf{z}'} &\leftarrow \Delta z_1 \Delta z_2 H(\mathbf{z}, \mathbf{z}'),\end{aligned} \quad (56)$$

that yield the new discrete commutation relations and Hamiltonian

$$\begin{aligned}[B_{\mathbf{z}}, B_{\mathbf{z}'}^\dagger] &= \mathbb{I} \delta_{\mathbf{z}\mathbf{z}'} \leftarrow \mathbb{I} \Delta k_1 \Delta k_2 \delta^2(\mathbf{z} - \mathbf{z}') \\ H_{HP} &= \sum_{\mathbf{z}, \mathbf{z}'} B_{\mathbf{z}}^\dagger H_{\mathbf{z}\mathbf{z}'} B_{\mathbf{z}'}.\end{aligned} \quad (57)$$

Therefore, in summary, the relation between operators and the Hamiltonian matrix in the new lattice defined by the discretization of the coordinates $\mathbf{z}(\mathbf{k})$, with the original operators and Hamiltonian of the square lattice is:

$$\begin{aligned}B_{\mathbf{z}} &= \sqrt{D(\mathbf{z})} \frac{\Delta z_1 \Delta z_2}{\Delta k_x \Delta k_y} B_{\mathbf{k}} \\ H_{\mathbf{z}\mathbf{z}'} &= \sqrt{D(\mathbf{z}) D(\mathbf{z}')} \frac{\Delta z_1 \Delta z_2}{\Delta k_x \Delta k_y} H_{\mathbf{k}\mathbf{k}'}\end{aligned} \quad (58)$$

The idea is that the Hamiltonian H_{HP} in Eq. (57) will produce the same physical results as the one in the square lattice in Eq. (26) of the main text in the thermodynamic limit.

B. Polar re-discretization

We choose $\mathbf{z} = (k, \phi)$ where k is the radius of the momentum vector and ϕ its polar angle. We then discretize

the radial direction in two different ways specified below to check numerically that the precise form of the discretization is not crucial to the results. Therefore we choose the radial coordinate as:

$$k = k(\theta) \rightarrow k_n = k(\theta_n, \Delta\theta), \quad (59)$$

where θ is another parameter labeling the radial coordinate that we will choose to be uniformly discretized. The corresponding Jacobian for this parametrization is:

$$D(\theta) = k(\theta) \frac{dk(\theta)}{d\theta}. \quad (60)$$

The parameters θ and ϕ are uniformly discretized as follows:

$$\begin{aligned}\theta_n &= n\Delta\theta, \quad m \in \{1, \dots, N\}, \\ \phi_l &= l\Delta\phi, \quad n \in \{-L, \dots, L\},\end{aligned} \quad (61)$$

where N is the total number of slices of the radial coordinate and $2L + 1$ is the total number of slices for the angular coordinate, and

$$\Delta\theta = \Delta\theta(N), \quad \Delta\phi = \frac{2\pi}{2L + 1}. \quad (62)$$

The actual form of $k(\theta_n, \Delta\theta)$ is determined by the particular discretization used to calculate the matrix elements of the Hamiltonian (more details in §VII A). Therefore, the new polar lattice is determined by the sites $\mathbf{z} = (k_n, \phi_l)$ where:

$$k_n = k(n, \Delta\theta), \quad \phi_l = l\Delta\phi, \quad (63)$$

After replacing (59) and (60) into (58) we get the expression for $B_{\mathbf{k}}$ and $H_{\mathbf{k}\mathbf{k}'}$ in the polar lattice

$$\begin{aligned}B_n^l &= \frac{\mathcal{K}\sqrt{A}}{2\pi} \sqrt{\Delta\theta \Delta\phi D_n} B_{\mathbf{k}_{nl}}^\dagger, \\ H_{nn'}^{ll'} &= \frac{\mathcal{K}^2 A}{(2\pi)^2} \Delta\theta \Delta\phi \sqrt{D_n D_{n'}} H_{\mathbf{k}_{nl} \mathbf{k}_{n'l'}},\end{aligned} \quad (64)$$

where $D_n = D(n\Delta\theta)$ and $\mathbf{k}_{nl} = \mathbf{k}(\theta_n, \phi_l)$. Finally, the whole Hamiltonian is

$$H_{HP} = \sum_{nl} \sum_{n'l'} B_n^{\dagger l} H_{nn'}^{ll'} B_{n'}^{l'}. \quad (65)$$



FIG. 7. Depiction of the re-discretization procedure, from the initial square through the continuum limit of the system to the polar lattice and the integration of the angular coordinate in angular momentum channels reducing the dimensionality of the system to 1.

C. Angular momentum channels

Because the Hamiltonian matrix $H_{\mathbf{k}\mathbf{k}'}$ that enters into the Hamiltonian H_{HP} in Eq. (26) of the main text only depends on the difference between the polar angles $\phi - \phi'$ we have conservation of the angular momentum l of the bosons. Consequently, we perform Fourier transforms on the polar angles for the fields B_{mn} and the matrix $H_{mn,m'n'}$

$$B_n^l = \frac{1}{\sqrt{2L+1}} \sum_{\ell=-L}^L e^{-i\ell\phi_l} B_n^\ell, \quad (66)$$

$$H_{nn'}^{ll'} = \sum_{\ell=-L}^L e^{-i\ell(\phi_l - \phi_{l'})} H_{nn'}^\ell, \quad (67)$$

such that the total Bogoliubov Hamiltonian decomposes into a direct sum for different angular momentum channels, as follows:

$$H_{HP} = \sum_{nn'\ell} B_n^{\ell\dagger} H_{nn'}^\ell B_{n'}^\ell. \quad (67)$$

In that way, each dataset obtained from diagonalizing a $2N \times 2N$ matrix is labelled by the coupling constant g_K and spreading a_K of the Gaussian potential, the number of layers $m = 2$ fixed for bilayer graphene, the angular momentum ℓ and the number of sites in the radial coordinate N .

VII. NUMERICAL RESULTS

A. Description of the numerical procedure

The solution of the system is found with exact diagonalization of the $2N \times 2N$ matrix composed by the matrix elements of the Hamiltonian for the hopping ($b_{k_1}^\dagger b_{k_2}$) and pairing ($b_{k_1} b_{k_2}$, $b_{k_1}^\dagger b_{k_2}^\dagger$) terms. The parameters of the Hamiltonian are:

- Angular momentum $\ell = 0, 1, 2, 3, 4, 5$.
- Coupling constant $a_K = 1, 2, 5, 10$.
- Reciprocal spreading $a_K = 1, 2, 5, 10$.
- System size $N = 100, 200, 300, 400, 500$.

and the UV-cutoff being set to the unity, i.e., $K = 1$ and $E_{UV} = 1$.

Regarding the spacing of the lattice for the radial component of the momentum $k_n = k(\theta_n, \Delta\theta)$, the following four parametrizations were taken into account to show that at the infinite size limit $N \rightarrow \infty$ the results do not depend on the discretization:

- Discretization by powers of n ($R = 1, 2$):

$$k_n = K (n\Delta\theta)^R, \quad (68)$$

with Jacobian given by

$$D_n = K^2 R \Delta k (n\Delta\theta)^{2R-1}, \quad (69)$$

and spacing

$$\Delta\theta = 1/N. \quad (70)$$

- Discretization by tangent of n ($R = 1, 2$):

$$k_n = \frac{K}{\sqrt{R}} \tan^R (n\Delta\theta) \quad (71)$$

with Jacobian given by

$$D_n = K^2 \Delta\theta \sec^2 (n\Delta\theta) \tan^{2R-1} (n\Delta\theta), \quad (72)$$

and spacing

$$\Delta\theta = \frac{\pi/2}{N+1} \quad (73)$$

Consequently, the Hamiltonians spanned by the parameter space $\{\ell, g_K, a_K, N, R\}$ are obtained using the parametrizations of the radial coordinate k_n , then the infinite size limit $N \rightarrow \infty$ is taken to ensure that the results are independent of the particular discretization chosen during the numerical procedures.

B. Imaginary eigenvalues after doing exact diagonalization

The Hamiltonian was diagonalized for the different sets of the parameter space $\{\ell, g_K, a_K, N, R\}$, and then the energy spectra were examined looking for non-vanishing imaginary parts $\text{Im}[E(k)]$ pointing out to an instability in the modes of the system. The only two angular momentum channels that got non-vanishing imaginary parts in their eigenvalue spectra were $\ell = 0$ and $\ell = 2$, both showing only one eigenvalue with imaginary part (with the corresponding complementary eigenvalue with the opposite sign) at the site $n = 1$, corresponding to the smallest momentum,

$$\text{Im}[E(k_{\min})] = \text{Im}[E(\Delta\theta)] \neq 0, \quad (74)$$

shown in the Figs. 8 and 9 for $\ell = 0$ and $\ell = 2$, respectively. Since the imaginary eigenvalues show a finite asymptotic trend when $k_{\min} \rightarrow 0$, i.e., $N \rightarrow \infty$, the five values obtained for each system size are taken to get the infinite size limit shown as the circles \circ in the forementioned figures.

As expected, although the four discretizations of k_n yield different numerical results depending on the power R , the form of $k(n, \Delta k)$ (powers in Eq. (68) or tangents in Eq. (71)), or the system size N , the infinite system size limit $N \rightarrow \infty$ where $k_1 \rightarrow 0$ yields almost the same imaginary eigenvalues, with a slight increment for the

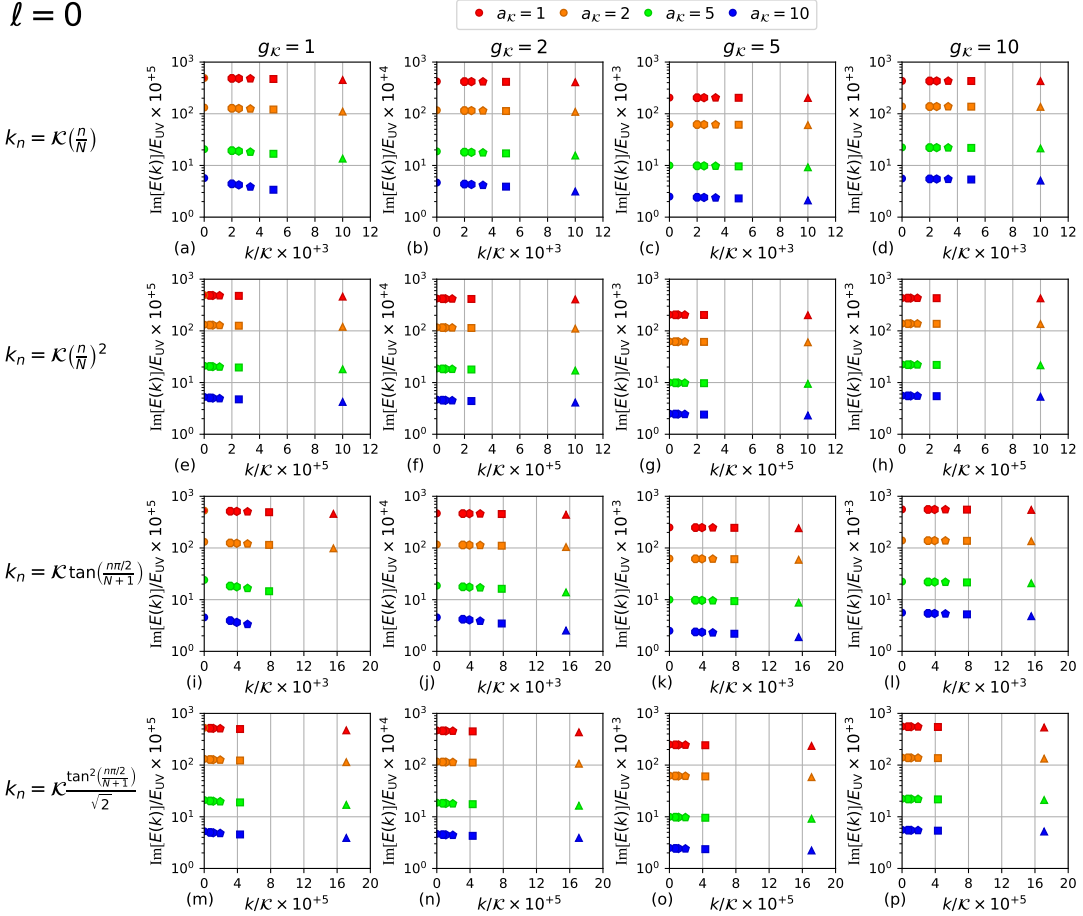


FIG. 8. Imaginary parts of the eigenvalues corresponding to the smallest momentum k_1 for $\ell = 0$ and different system sizes N : \triangle ($N = 100$), \square ($N = 200$), \diamond ($N = 300$), \circ ($N = 400$), and \circ ($N = 500$). The extrapolation is \circ for $N \rightarrow \infty$.

tangent discretization produced by the contribution of the sites along the radial momentum beyond the UV-cut-off K , in other words, the sites k_n with $n > N/2$.

There are some plots for small g_K with $R = 1$ like Fig. 8(a) or 8(c), or even worse in Fig. 9(a) and 9(c) where there are missing markers for large a_K that are shown in their analogues with $R = 2$, Figs. 8(b), 8(d), 9(b) and 9(d), respectively. This fact suggests that finer lattices are required to catch the non-vanishing imaginary part of the eigenvalue corresponding to the site with the smallest momentum, k_1 , supporting the fact that the imaginary eigenvalue, i.e., the instability, is located at momentum $k \rightarrow 0$.

The main differences between $\ell = 0$ and $\ell = 2$ channels root on the relative size of their imaginary eigenvalues, being smaller for the latter channel, almost a half of those ones for the former channel. On the other hand, the channels show expected behaviors like the increasing of $\text{Im}[E(k_{\min})]$ for larger g_K , i.e., stronger interactions, and the suppression for larger a_K , that is, a wider spreading of the potential, turning out in a weaker interaction and consequently, smaller values for $\text{Im}[E(k_{\min})]$.

The infinite size limits for $\text{Im}[E(k_{\min} \rightarrow 0)]$, from now

on denoted as $\text{Im}[E^\ell](a_K, g_K)$, are obtained using the dataset found with the tangent discretization in Eq. (71) with $R = 3$ and least-squares on the Ansatz

$$\text{Im}[E^\ell](a_K, g_K, N) = \text{Im}[E^\ell](a_K, g_K) + \frac{\Delta \text{Im}[E^\ell](a_K, g_K)}{N}. \quad (75)$$

The results are listed in the tables II and III for the channels $\ell = 0$ and $\ell = 2$, respectively, and are summarized in the Fig. 10 for large coupling $g_K \geq 1$.

C. Ansatz

The first Ansatz proposed by Inti consisted in the following function:

$$\text{Im}[E^\ell](a_K, g_K) = C_\ell(a_K) e^{-G_\ell(a_K)/g_K}, \quad (76)$$

where $G_\ell(a_K)$ and $C_\ell(a_K)$ are parameters to be found for each set of points labelled with a_K . The points used for the fitting are the infinite-size limits $\text{Im}[E^\ell](a_K, g_K)$ listed in the tables II and III. The table I shows the results of

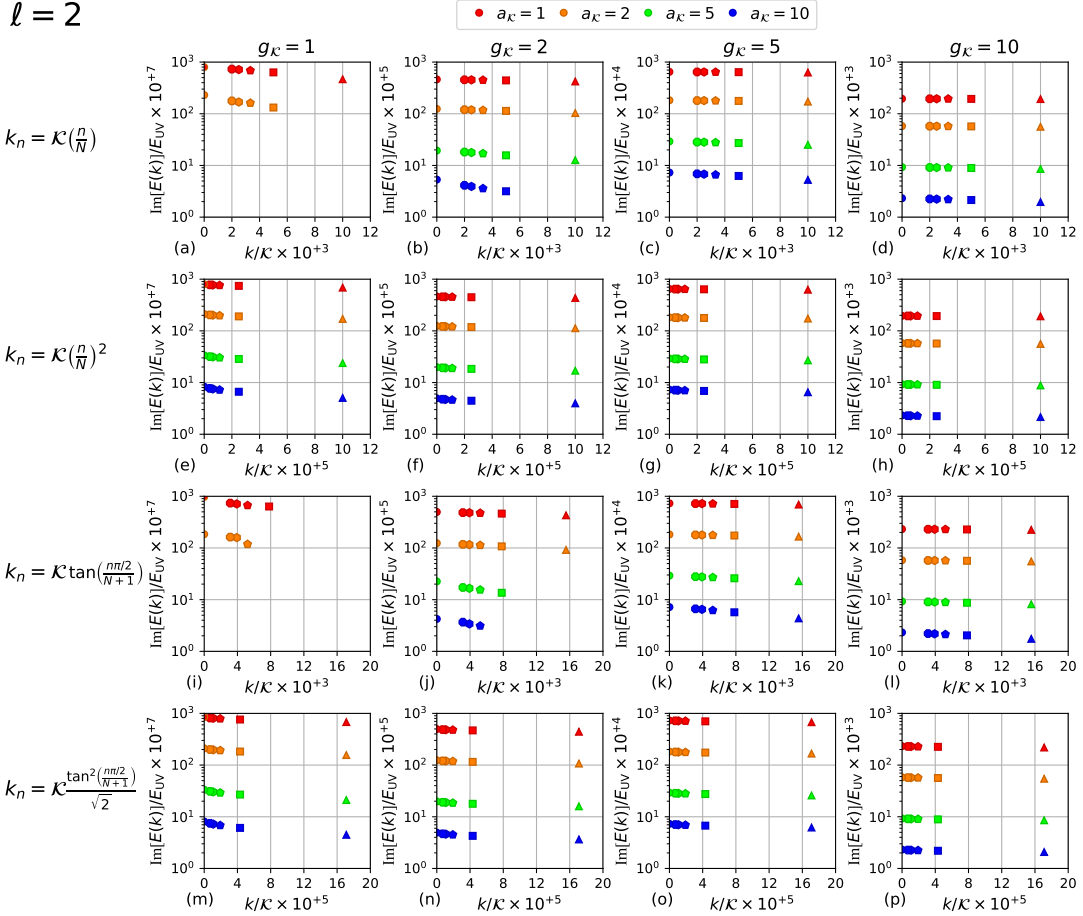


FIG. 9. Imaginary parts of the eigenvalues corresponding to the smallest momentum k_1 for $\ell = 2$ and different system sizes N : \triangle ($N = 100$), \square ($N = 200$), \diamond ($N = 300$), \circ ($N = 400$), and \bigcirc ($N = 500$). The extrapolation is \bigcirc for $N \rightarrow \infty$.

	$\ell = 0$		$\ell = 2$	
a_K	C_0	G_0	C_2	G_2
1	$(2.805 \pm 0.020) \times 10^{-1}$	4.020 ± 0.003	$(2.619 \pm 0.004) \times 10^{-1}$	8.042 ± 0.001
2	$(7.116 \pm 0.062) \times 10^{-2}$	4.028 ± 0.004	$(6.697 \pm 0.073) \times 10^{-2}$	8.063 ± 0.008
3	$(3.158 \pm 0.014) \times 10^{-2}$	4.027 ± 0.002	$(2.967 \pm 0.019) \times 10^{-2}$	8.062 ± 0.005
5	$(1.113 \pm 0.013) \times 10^{-2}$	4.024 ± 0.004	$(1.078 \pm 0.008) \times 10^{-2}$	8.073 ± 0.005
7	$(5.862 \pm 0.058) \times 10^{-3}$	4.035 ± 0.004	$(5.548 \pm 0.101) \times 10^{-3}$	8.082 ± 0.014
10	$(2.917 \pm 0.040) \times 10^{-3}$	4.044 ± 0.006	$(2.783 \pm 0.056) \times 10^{-3}$	8.106 ± 0.002

TABLE I. Fitting of parameters C_0 and G_0 depending on a_K to the first Ansatz in Eq. (76).

the fitting of the Eq. (76) using non-linear least-squares (NLLS), and are summarized in the Fig. 11.

In order to improve the first Ansatz, the two parameters $G_\ell(a_K)$ and $C_\ell(a_K)$ were fitted by a second NLLS procedure on two Ansätze. The first one for $G_\ell(a_K)$ given by

$$G_\ell(a_K) = G_\ell + a_K \Delta G_\ell \quad (77)$$

yielding the parameters

$$\begin{aligned} G_0 &= 4.020 \pm 0.002, \\ \Delta G_0 &= (2.110 \pm 0.645) \times 10^{-3}, \end{aligned} \quad (78)$$

in the channel $\ell = 0$, and

$$\begin{aligned} G_2 &= 8.034 \pm 0.002, \\ \Delta G_2 &= (7.782 \pm 0.839) \times 10^{-3}, \end{aligned} \quad (79)$$

in the channel $\ell = 2$. Since the slope of the fittings ΔG_ℓ are three orders of magnitude smaller than the intercept and $a_K \sim 1$, we can assume that G_ℓ is constant respect to a_K (see Fig. 12(b)). Meanwhile the Ansatz for $C_\ell(a_K)$ is a power law

$$C_\ell(a_K) = \left(\frac{A_\ell}{a_K} \right)^{\alpha_\ell}, \quad (80)$$

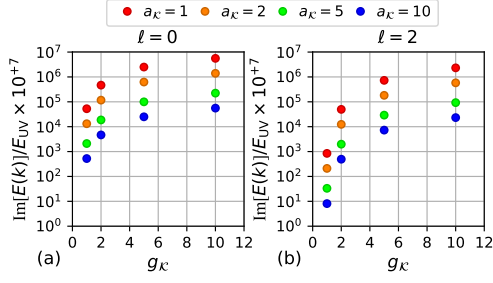


FIG. 10. Summarize of the infinite size limit $N \rightarrow \infty$ of the imaginary parts shown in Figs. 8 and 9 vs. the coupling constant g_K .

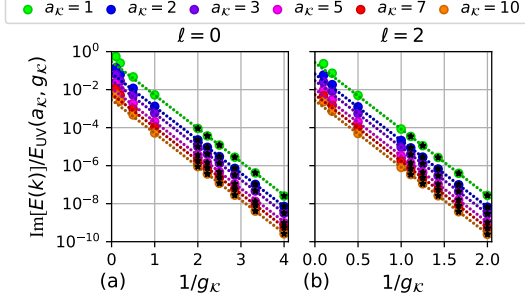


FIG. 11. Infinite-size limits $\text{Im}[E^\ell](a_K, g_K)$ vs. $1/g_K$ compared to the fitted Ansatz shown in Eq. (76). The points used in the interpolation are highlighted with black stars. Notice the discrepancy at strong coupling $g_K \geq 1$.

whose parameters found are

$$\begin{aligned} A_0 &= (5.282 \pm 0.029) \times 10^{-1}, \\ \alpha_0 &= 1.990 \pm 0.006, \end{aligned} \quad (81)$$

in the channel $\ell = 0$, and

$$\begin{aligned} A_2 &= (5.084 \pm 0.005) \times 10^{-1}, \\ \alpha_2 &= 1.981 \pm 0.002, \end{aligned} \quad (82)$$

in the channel $\ell = 2$. The small errors of the parameters after the fitting suggest us that the power-law is a good Ansatz to describe $C_\ell(a_K)$ (see Fig. 12(a)).

Therefore, Inti's Ansatz was modified to include the new power law with $\alpha = 2$ as follows:

$$\text{Im}[E^\ell](a_K, g_K) = \left(\frac{A_\ell}{a_K} \right)^2 e^{-G_\ell/g_K}, \quad (83)$$

and then fitted using two-dimensional NLLS on the plane (a_K, g_K) yielding that

$$\begin{aligned} A_0 &= (5.306 \pm 0.015) \times 10^{-1}, \\ G_0 &= 4.024 \pm 0.002, \end{aligned} \quad (84)$$

in the channel $\ell = 0$, and

$$\begin{aligned} A_2 &= (5.135 \pm 0.018) \times 10^{-1}, \\ G_2 &= 8.050 \pm 0.005, \end{aligned} \quad (85)$$

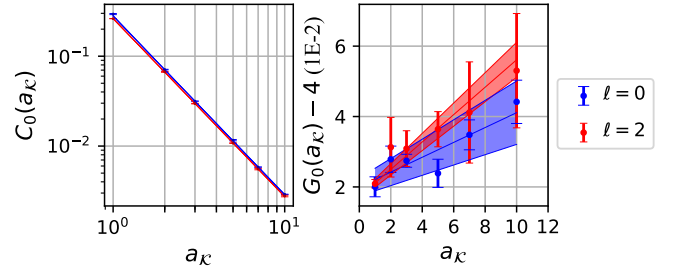


FIG. 12. Data points shown in the Tab. I and fitted Ansätze. Left: C_0 vs. a_K : the power law in Eq. (80) was fitted with the parameters in Eqs. (81) and (82) for $\ell = 0$ and $\ell = 2$. Right: G_0 vs. a_K : the linear regression yielded the parameters in Eq. (78) and (79) (the data for $\ell = 2$ was divided by 2 to ease the interpretation of the plot). Both figures include the error bars as well as the regions allowed by the standard errors of the fittings.

in the channel $\ell = 2$. The fitted data as well as the Ansatz of Eq. (83) are shown in the Fig. 13 including projections onto the planes $\text{Im}[E^\ell](a_K, g_K)$ vs. $1/g_K$ and $\text{Im}[E^\ell](a_K, g_K)$ vs. a_K .

Lastly, the fitting also suggests a relation in the G_ℓ parameters, corresponding to the power of the exponential in Eq. (83), that $G_2 = 2G_0$, which is consistent to the standard errors reported above. A similar conclusion may not be done on A_ℓ since the standard errors as well as the central values do not allow such overlapping.

VIII. INTI'S GENERAL SCHEME

The system without interactions is described by the following 2D Hamiltonian

$$H_{\text{kin}} = \int d^2r \Psi_{\mathbf{r}}^\dagger \left(\boldsymbol{\sigma} \cdot \frac{\nabla}{i} \right) \Psi_{\mathbf{r}} = \sum_{\mathbf{k}} \Psi_{\mathbf{k}}^\dagger (\boldsymbol{\sigma} \cdot \mathbf{k}) \Psi_{\mathbf{k}} \quad (86)$$

where $\Psi_{\mathbf{k}}$ is the annihilation operator of the fundamental representation of $\text{SU}(2)$

$$\Psi_{\mathbf{k}} = \begin{pmatrix} \psi_{\mathbf{k}\uparrow} \\ \psi_{\mathbf{k}\downarrow} \end{pmatrix}, \quad (87)$$

and the occupied state is given by the action of the creation operator on the ground state

$$|\mathbf{k}\sigma\rangle = \psi_{\mathbf{k}\sigma}^\dagger |0\rangle \quad (88)$$

whose time evolution is determined by the Hamiltonian

$$i \frac{\partial}{\partial t} |\mathbf{k}\sigma\rangle = H |\mathbf{k}\sigma\rangle \quad (89)$$

The Lagrangian associated to the Hamiltonian is given by

$$L = i \left\langle \mathbf{k}\sigma \left| \frac{\partial}{\partial t} \right| \mathbf{k}\sigma \right\rangle - \left\langle \mathbf{k}\sigma \left| H \right| \mathbf{k}\sigma \right\rangle \quad (90)$$

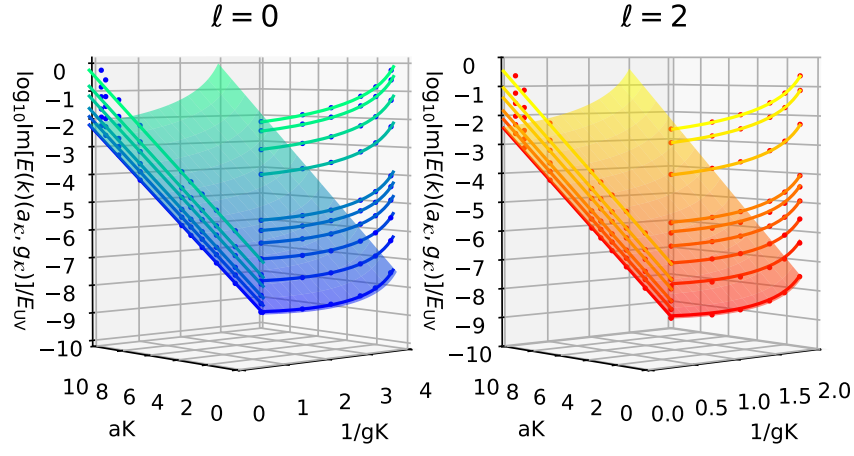


FIG. 13. Infinite-size limits $\text{Im}[E^\ell](a_K, g_K)$ vs. the inverse of the coupling constant $1/g_K$ with the fitted Ansatz shown in Eq. (76). The points used in the interpolation are highlighted with black stars. Notice the discrepancy at strong coupling $g_K \geq 1$.

The following operator rotates the spins at every given momentum \mathbf{k} around the axis $\hat{\Omega}$ by an angle $|\Omega|$:

$$\begin{aligned} U(\Omega(\mathbf{k})) &= \exp \left[\frac{i}{2} \sum_{\mathbf{k}} \Omega(\mathbf{k}) \cdot \mathbf{S}_{\mathbf{k}} \right] \\ &= \exp \left[\frac{i}{2} \sum_{\mathbf{k}} \Omega(\mathbf{k}) \cdot (\Psi_{\mathbf{k}}^\dagger \boldsymbol{\sigma} \Psi_{\mathbf{k}}) \right] \end{aligned} \quad (91)$$

where $\mathbf{S}_{\mathbf{k}} = \Psi_{\mathbf{k}}^\dagger \boldsymbol{\sigma} \Psi_{\mathbf{k}}$ is the spin operator. Consider the case of a single spin $1/2$

$$U(\Omega(\mathbf{k})) = \exp \left[\frac{i}{2} \Omega \cdot (\Psi^\dagger \boldsymbol{\sigma} \Psi) \right] \quad (92)$$

The action of $U(\Omega)$ on σ_i is obtained using the well-known Baker-Campbell-Hausdorff formula (BCH):

$$\begin{aligned} U^\dagger(\Omega) \sigma_i U(\Omega) &\approx \\ &\approx \sigma_i - \frac{i}{2} \Omega^j [\sigma_j, \sigma_i] + \left(\frac{-i}{2} \right)^2 \frac{\Omega^j \Omega^k}{2!} [\sigma_j, [\sigma_k, \sigma_i]] \\ &= \sigma_i - \frac{i}{2} \Omega^j 2i \epsilon_{ji}^k \sigma_k + \left(\frac{-i}{2} \right)^2 \frac{\Omega^j \Omega^k}{2!} [\sigma_j, 2i \epsilon_{ki}^l \sigma_l] \\ &= \sigma_i + \Omega^j \epsilon_{ji}^k \sigma_k + \frac{\Omega^j \Omega^k}{2!} \epsilon_{ki}^l \epsilon_{jl}^m \sigma_m, \end{aligned} \quad (93)$$

which in vector notation can be expressed as

$$\begin{aligned} U^\dagger(\Omega) \boldsymbol{\sigma} U(\Omega) &= \\ &= \boldsymbol{\sigma} + \boldsymbol{\sigma} \times \boldsymbol{\Omega} + \frac{1}{2!} (\boldsymbol{\sigma} \times \boldsymbol{\Omega}) \times \boldsymbol{\Omega} + \dots \\ &= \sum_{n=0}^{\infty} \frac{1}{n!} \left(\dots (\underbrace{\boldsymbol{\sigma} \times \boldsymbol{\Omega}}_{n \text{ times}}) \dots \right) \times \boldsymbol{\Omega} \end{aligned} \quad (94)$$

The spin-up state is defined as $\mathbf{s}|\uparrow\rangle = \hat{\mathbf{z}}|\uparrow\rangle$ while the spin-down is $\mathbf{s}|\downarrow\rangle = -\hat{\mathbf{z}}|\downarrow\rangle$. Then, the matrix element

$\langle \uparrow \uparrow \rangle$ of $\boldsymbol{\sigma}$ is given by

$$\langle \uparrow | \sigma_i | \uparrow \rangle = \text{Tr} \left(\frac{1 + \mathbf{z} \cdot \boldsymbol{\sigma}}{2} \sigma_i \right) = \frac{z^i}{2} \text{Tr}(\sigma_j \sigma_i) = z_i, \quad (95)$$

and similarly $\langle \downarrow | \sigma_i | \downarrow \rangle = -z_i$

$$\langle \uparrow | U^\dagger(\Omega) \boldsymbol{\sigma} U(\Omega) | \uparrow \rangle = \sum_{n=0}^{\infty} \frac{1}{n!} \left(\dots (\underbrace{\mathbf{z} \times \boldsymbol{\Omega}}_{n \text{ times}}) \dots \right) \times \boldsymbol{\Omega} \quad (96)$$

The Berry phase part

$$i \left\langle \uparrow \left| U^\dagger(\Omega) \frac{d}{dt} U(\Omega) \right| \uparrow \right\rangle = ? \quad (97)$$

can be obtained with a modified BCH formula

$$\begin{aligned} U^\dagger(\Omega) \frac{d}{dt} U(\Omega) &\approx \\ &\approx \frac{i}{2} \frac{d\Omega}{dt} \cdot \boldsymbol{\sigma} + \frac{1}{2!} \left[\frac{i}{2} \frac{d\Omega}{dt} \cdot \boldsymbol{\sigma}, \frac{i}{2} \Omega \cdot \boldsymbol{\sigma} \right] \\ &= \frac{i}{2} \frac{d\Omega^i}{dt} \sigma_i + \frac{1}{2!} \left(\frac{i}{2} \right)^2 \frac{d\Omega^i}{dt} \Omega^j [\sigma_i, \sigma_j] \\ &= \frac{i}{2} \frac{d\Omega^i}{dt} \sigma_i + \frac{1}{2!} \left(\frac{i}{2} \right)^2 \frac{d\Omega^i}{dt} \Omega^j 2i \epsilon_{ij}^k \sigma_k \\ &= \frac{i}{2} \frac{d\Omega^i}{dt} \sigma_i - \frac{1}{2!} \left(\frac{i}{2} \right) \frac{d\Omega^i}{dt} \Omega^j \epsilon_{ij}^k \sigma_k \end{aligned} \quad (98)$$

which

$$\begin{aligned} i U^\dagger(\Omega) \frac{d}{dt} U(\Omega) &= \\ &= - \left(\frac{1}{2} \right) \frac{d\Omega}{dt} \cdot \boldsymbol{\sigma} + \left(\frac{1}{2} \right) \frac{1}{2!} \left(\frac{d\Omega}{dt} \times \boldsymbol{\Omega} \right) \cdot \boldsymbol{\sigma} + \dots \\ &= \frac{1}{2} \sum_{n=1}^{\infty} \frac{(-1)^n}{n!} \left(\dots \left(\frac{d\Omega}{dt} \times \boldsymbol{\Omega} \right) \dots \right) \times \boldsymbol{\Omega} \cdot \boldsymbol{\sigma} \end{aligned} \quad (99)$$

The semiclassical Lagrangian is therefore expressed as follows:

$$\begin{aligned} \mathcal{L}[\Omega] &= i \left\langle \uparrow \left| U^\dagger(\Omega) \frac{d}{dt} U(\Omega) \right| \uparrow \right\rangle - \left\langle \uparrow \left| U^\dagger(\Omega) \boldsymbol{\sigma} \cdot \mathbf{k} U(\Omega) \right| \uparrow \right\rangle \\ &= -\frac{1}{2} \frac{d\Omega}{dt} \cdot \mathbf{z} + \frac{1}{4} \left(\frac{d\Omega}{dt} \times \Omega \right) \cdot \mathbf{z} + \boldsymbol{\sigma} \cdot \boldsymbol{\Omega} + \frac{1}{2!} (\boldsymbol{\sigma} \times \Omega) \cdot \mathbf{z} \end{aligned}$$

Lorem ipsum dolor sit amet, consectetur adipiscing elit. Quisque eu pharetra ligula, in scelerisque risus. Mauris convallis neque elit, at tincidunt lectus venenatis et. Donec ultricies eros nec nisl posuere, vitae scelerisque enim fringilla. Maecenas eget odio dapibus, egestas ante a, tempor neque. Nullam in nisi varius, laoreet urna sit amet, hendrerit erat. Maecenas id ligula posuere, tincidunt nisi a, scelerisque libero. Quisque maximus quis sem eleifend fermentum. Ut pharetra dui quis pharetra consectetur. Pellentesque commodo lacinia urna. Aliquam nibh nulla, facilisis id cursus eget, tristique non neque.

Proin risus sem, viverra vitae ornare ut, imperdiet a erat. Ut aliquet lorem sit amet elit efficitur auctor. Praesent consequat magna a neque feugiat, eget facilisis sem eleifend. Proin id posuere est, nec sodales nibh. Maecenas lacus felis, fringilla eu ligula at, gravida feugiat orci. In id faucibus massa. Phasellus iaculis iaculis mauris, vitae congue orci hendrerit eu. Proin interdum nisl at justo scelerisque ullamcorper. Maecenas tincidunt lectus quis gravida faucibus. Vestibulum tempor fermentum egestas.

Lorem ipsum dolor sit amet, consectetur adipiscing elit. Quisque eu pharetra ligula, in scelerisque risus. Mauris convallis neque elit, at tincidunt lectus venenatis et. Donec ultricies eros nec nisl posuere, vitae scelerisque enim fringilla. Maecenas eget odio dapibus, egestas ante a, tempor neque. Nullam in nisi varius, laoreet urna sit amet, hendrerit erat. Maecenas id ligula posuere, tincidunt nisi a, scelerisque libero. Quisque maximus quis sem eleifend fermentum. Ut pharetra dui quis pharetra consectetur. Pellentesque commodo lacinia urna. Aliquam nibh nulla, facilisis id cursus eget, tristique non neque.

Lorem ipsum dolor sit amet, consectetur adipiscing elit. Quisque eu pharetra ligula, in scelerisque risus. Mauris convallis neque elit, at tincidunt lectus venenatis et. Donec ultricies eros nec nisl posuere, vitae scelerisque enim fringilla. Maecenas eget odio dapibus, egestas ante a, tempor neque. Nullam in nisi varius, laoreet urna sit amet, hendrerit erat. Maecenas id ligula posuere, tincidunt nisi a, scelerisque libero. Quisque maximus quis sem eleifend fermentum. Ut pharetra dui quis pharetra consectetur. Pellentesque commodo lacinia urna. Aliquam nibh nulla, facilisis id cursus eget, tristique non neque.

Appendix A: Infinite limits

Lorem ipsum dolor sit amet, consectetur adipiscing elit. Quisque eu pharetra ligula, in scelerisque risus.

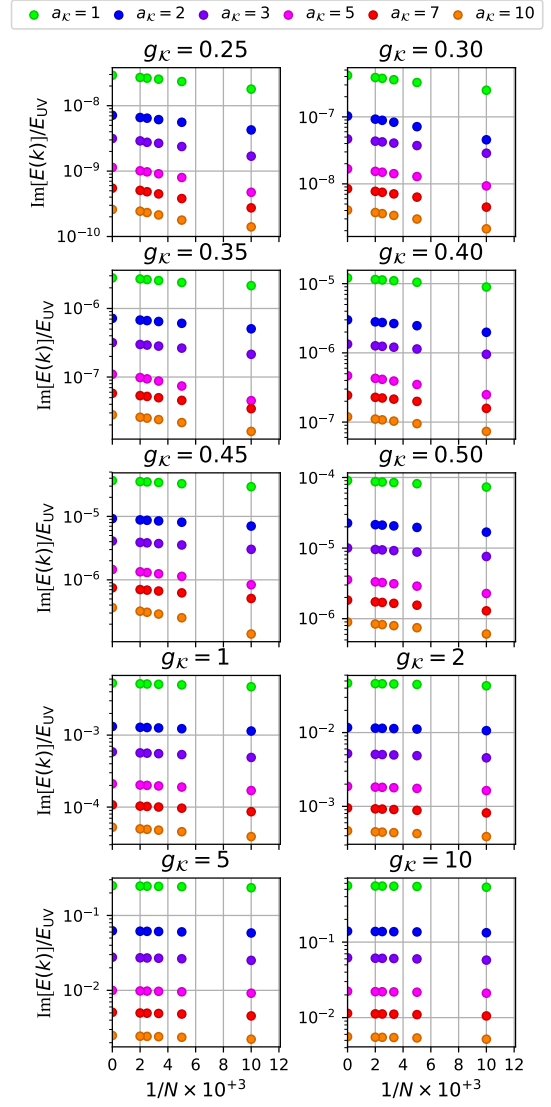


FIG. 14. Extrapolation of the imaginary parts in the channel $\ell = 0$ as the linear regression given in Eq. (75) for five different system sizes $N = 100, 200, 300, 400$ and 500 . The infinite-size limits are listed with their standard errors in Tab. II.

Mauris convallis neque elit, at tincidunt lectus venenatis et. Donec ultricies eros nec nisl posuere, vitae scelerisque enim fringilla. Maecenas eget odio dapibus, egestas ante a, tempor neque. Nullam in nisi varius, laoreet urna sit amet, hendrerit erat. Maecenas id ligula posuere, tincidunt nisi a, scelerisque libero. Quisque maximus quis sem eleifend fermentum. Ut pharetra dui quis pharetra consectetur. Pellentesque commodo lacinia urna. Aliquam nibh nulla, facilisis id cursus eget, tristique non neque.

Lorem ipsum dolor sit amet, consectetur adipiscing elit. Quisque eu pharetra ligula, in scelerisque risus. Mauris convallis neque elit, at tincidunt lectus venenatis et. Donec ultricies eros nec nisl posuere, vitae scelerisque enim fringilla. Maecenas eget odio dapibus, egestas ante a, tempor neque. Nullam in nisi varius, laoreet urna sit

a_K	$1/g_K$	$\text{Im}[E^{(0)}](a_K, g_K)$
1	4.	$(2.92152 \pm 0.00789) \times 10^{-8}$
1	3.33333	$(4.16824 \pm 0.03815) \times 10^{-7}$
1	2.85714	$(2.78958 \pm 0.04014) \times 10^{-6}$
1	2.5	$(1.20918 \pm 0.00247) \times 10^{-5}$
1	2.22222	$(3.67784 \pm 0.13941) \times 10^{-6}$
1	2.	$(9.05161 \pm 0.11104) \times 10^{-6}$
<hr/>		
2	4.	$(7.13223 \pm 0.05980) \times 10^{-9}$
2	3.33333	$(1.02927 \pm 0.01370) \times 10^{-7}$
2	2.85714	$(7.17900 \pm 0.02154) \times 10^{-7}$
2	2.5	$(2.99848 \pm 0.01200) \times 10^{-6}$
2	2.22222	$(9.23142 \pm 0.01736) \times 10^{-6}$
2	2.	$(2.25623 \pm 0.04265) \times 10^{-6}$
<hr/>		
3	4.	$(3.15043 \pm 0.03078) \times 10^{-9}$
3	3.33333	$(4.68115 \pm 0.02323) \times 10^{-8}$
3	2.85714	$(3.18026 \pm 0.01185) \times 10^{-7}$
3	2.5	$(1.33870 \pm 0.00375) \times 10^{-6}$
3	2.22222	$(4.09552 \pm 0.00318) \times 10^{-6}$
3	2.	$(1.00257 \pm 0.01928) \times 10^{-6}$
<hr/>		
5	4.	$(1.13815 \pm 0.00536) \times 10^{-9}$
5	3.33333	$(1.67524 \pm 0.00993) \times 10^{-8}$
5	2.85714	$(1.09754 \pm 0.01789) \times 10^{-7}$
5	2.5	$(4.67946 \pm 0.04882) \times 10^{-7}$
5	2.22222	$(1.45688 \pm 0.00646) \times 10^{-6}$
5	2.	$(3.56892 \pm 0.01652) \times 10^{-6}$
<hr/>		
7	4.	$(5.48481 \pm 0.15749) \times 10^{-10}$
7	3.33333	$(8.46152 \pm 0.07365) \times 10^{-9}$
7	2.85714	$(5.79094 \pm 0.03126) \times 10^{-8}$
7	2.5	$(2.44125 \pm 0.01064) \times 10^{-7}$
7	2.22222	$(7.47993 \pm 0.02632) \times 10^{-7}$
7	2.	$(1.83301 \pm 0.00538) \times 10^{-6}$
<hr/>		
10	4.	$(2.59171 \pm 0.10806) \times 10^{-10}$
10	3.33333	$(4.06583 \pm 0.05989) \times 10^{-9}$
10	2.85714	$(2.81035 \pm 0.02282) \times 10^{-8}$
10	2.5	$(1.19031 \pm 0.00658) \times 10^{-7}$
10	2.22222	$(3.64543 \pm 0.00559) \times 10^{-7}$
10	2.	$(8.95646 \pm 0.03185) \times 10^{-7}$

TABLE II. Infinite-size limits $\text{Im}[E^{(0)}](a_K, g_K)$ of the points on the plane a_K vs. $1/g_K$ extrapolated using least-squares on the Eq. (75) for the channel $\ell = 0$.

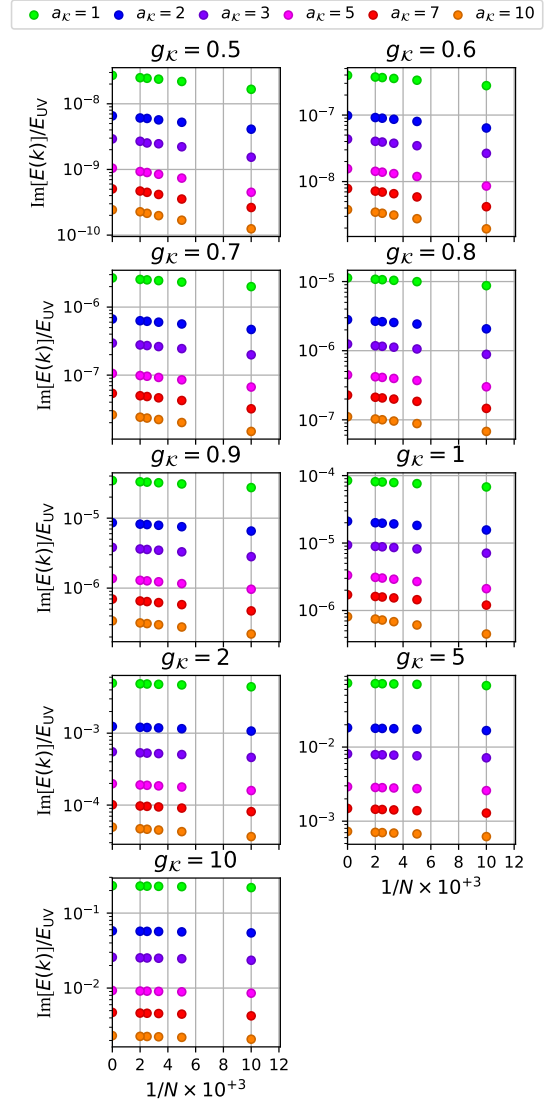


FIG. 15. Extrapolation of the imaginary parts in the channel $\ell = 2$ as the linear regression given in Eq. (75) for five different system sizes $N = 100, 200, 300, 400$ and 500 . The infinite-size limits are listed with their standard errors in Tab. III.

amet, hendrerit erat. Maecenas id ligula posuere, tincidunt nisi a, scelerisque libero. Quisque maximus quis sem eleifend fermentum. Ut pharetra dui quis pharetra consetetur. Pellentesque commodo lacinia urna. Aliquam nibh nulla, facilisis id cursus eget, tristique non neque.

Proin risus sem, viverra vitae ornare ut, imperdiet a erat. Ut aliquet lorem sit amet elit efficitur auctor. Praesent consequat magna a neque feugiat, eget facilisis sem eleifend. Proin id posuere est, nec sodales nibh. Maecenas lacus felis, fringilla eu ligula at, gravida feugiat orci. In id faucibus massa. Phasellus iaculis iaculis mauris, vitae congue orci hendrerit eu. Proin interdum nisl at justo scelerisque ullamcorper. Maecenas tincidunt lectus quis gravida faucibus. Vestibulum tempor fermentum egetas.

Proin vitae semper dolor. Etiam diam ex, lobortis vi-

$\ell = 2$		
a_K	$1/g_K$	$\text{Im}[E^{(2)}](a_K, g_K)$
1	2.	$(2.71270 \pm 0.00588) \times 10^{-8}$
1	1.66667	$(3.95448 \pm 0.01197) \times 10^{-7}$
1	1.42857	$(2.68217 \pm 0.00584) \times 10^{-6}$
1	1.25	$(1.12794 \pm 0.00193) \times 10^{-5}$
1	1.11111	$(3.45039 \pm 0.00493) \times 10^{-5}$
2	2.	$(6.55098 \pm 0.05278) \times 10^{-9}$
2	1.66667	$(9.81992 \pm 0.04536) \times 10^{-8}$
2	1.42857	$(6.67918 \pm 0.02030) \times 10^{-7}$
2	1.25	$(2.81190 \pm 0.00656) \times 10^{-6}$
2	1.11111	$(8.60731 \pm 0.01642) \times 10^{-6}$
3	2.	$(2.92241 \pm 0.02954) \times 10^{-9}$
3	1.66667	$(4.34776 \pm 0.02244) \times 10^{-8}$
3	1.42857	$(2.95870 \pm 0.01117) \times 10^{-7}$
3	1.25	$(1.24681 \pm 0.00355) \times 10^{-6}$
3	1.11111	$(3.81851 \pm 0.00882) \times 10^{-6}$
5	2.	$(1.04595 \pm 0.00465) \times 10^{-9}$
5	1.66667	$(1.55836 \pm 0.00861) \times 10^{-8}$
5	1.42857	$(1.05890 \pm 0.00543) \times 10^{-7}$
5	1.25	$(4.47072 \pm 0.01660) \times 10^{-7}$
5	1.11111	$(1.37043 \pm 0.00409) \times 10^{-6}$
7	2.	$(5.05321 \pm 0.15138) \times 10^{-10}$
7	1.66667	$(7.84517 \pm 0.07565) \times 10^{-9}$
7	1.42857	$(5.38602 \pm 0.02976) \times 10^{-8}$
7	1.25	$(2.27356 \pm 0.01000) \times 10^{-7}$
7	1.11111	$(6.97338 \pm 0.02489) \times 10^{-7}$
10	2.	$(2.42989 \pm 0.08010) \times 10^{-10}$
10	1.66667	$(3.78447 \pm 0.05330) \times 10^{-9}$
10	1.42857	$(2.61431 \pm 0.02132) \times 10^{-8}$
10	1.25	$(1.10834 \pm 0.00624) \times 10^{-7}$
10	1.11111	$(3.40468 \pm 0.01489) \times 10^{-7}$

TABLE III. Infinite-size limits $\text{Im}[E^{(2)}](a_K, g_K)$ of the points on the plane a_K vs. $1/g_K$ extrapolated using least-squares on the Eq. (75) for the channel $\ell = 2$.

tae rutrum sed, tempus at diam. Nunc ut felis mauris. Duis suscipit dui eu enim cursus, aliquet consequat est bibendum. Maecenas id enim consectetur, iaculis purus ac, consectetur quam. Suspendisse vel interdum turpis. Duis hendrerit tempor lacus, eu iaculis orci congue eu. Nam vitae tellus non nisi euismod feugiat vitae vitae ex. Quisque felis mauris, pulvinar sed dui sit amet, facilisis ultricies tortor. Quisque nibh massa, malesuada quis nisl sodales, faucibus semper ligula.

Duis imperdiet massa eu lacus fringilla, et pulvinar eros dapibus. Etiam dictum vulputate tempus. Integer felis dolor, mattis in tincidunt eu, sodales ac orci. Curabitur fermentum aliquam finibus. Praesent non dui nunc. Ut commodo vulputate lorem, nec pretium nisi lacinia vitae. Donec fermentum elementum ex vel mollis. Donec turpis nisi, placerat vel sollicitudin in, bibendum vel ipsum. Aliquam venenatis non nisl ut rutrum. Cras sed est tincidunt elit euismod fermentum et quis nisi. Ut fringilla ligula nisl, sed lobortis nunc laoreet et.

Morbi arcu leo, auctor ut luctus eu, eleifend sed lorem. Sed commodo molestie ligula ut tempor. Aenean posuere vel velit et ullamcorper. Integer consectetur semper arcu non hendrerit. Suspendisse ornare leo vel ornare sollicitudin. Vivamus elementum lacinia turpis quis suscipit. Duis varius aliquam tortor. Vestibulum ante ipsum primis in faucibus orci luctus et ultrices posuere cubilia curae; Morbi a tristique mauris. Quisque pretium, nibh in ornare elementum, neque velit efficitur dui, nec fermentum ipsum risus sit amet magna. Donec elit quam, cursus sed mollis non, aliquam vitae felis.